surfaces

MDPI

Article

Surface Plasmon Resonance-Based Temperature Sensor with Outer Surface Metal Coating on Multi-Core Photonic Crystal Fibre

Samuel Osifeso [1,†] [iD]**, Suoda Chu [1,†]** [iD]**, Ashwini Prasad [2] and K. Nakkeeran [1,*]** [iD]

[1]   School of Engineering, Fraser Noble Building, University of Aberdeen, Aberdeen AB24 3UE, UK; s.osifeso.19@abdn.ac.uk (S.O.); r05sc15@abdn.ac.uk (S.C.)
[2]   Analytically Vivid Limited, Edgbaston, Birmingham B16 9DT, UK; ashwiniprasad@analyticallyvivid.com
*   Correspondence: k.nakkeeran@abdn.ac.uk
†   These authors contributed equally to this work.

check for updates

Abstract: We report an innovative design of a multi-core photonic crystal fibre-based surface plasmon resonance temperature sensor using ethanol and benzene as temperature-sensitive materials with a segmented outer-surface metal coating scheme. A stable sensing performance for a detection range of 10–80 °C was found while using ethanol as the temperature-sensitive material; while using benzene both blue and red frequency shifts were observed. The maximum temperature sensitivities obtained from this proposed temperature sensor were 360 pm/°C and 23.3 nm/°C with resolutions of 2.78×10^{-1} °C and 4.29×10^{-3} °C, respectively, when using ethanol or benzene as the sensing medium.

Keywords: multi-core; photonic crystal fibre; surface plasmon resonance; temperature sensor; finite element method; surface metal coating

---

1. Introduction

In recent years, researchers have shown more interest in developing temperature sensors that are capable of remote sensing, easy to fabricate, light weight, economical, immune to electromagnetic interference or radiation [1] and so on. This is as a result of the significant role of temperature in various fields, such as environmental monitoring, manufacturing, medicine, quantum computing and many other applications.

In recent times, utilising photonic crystal fibres (PCFs) to fabricate temperature sensors has been reported quite frequently in the literature due to their compact size, reliability, structural flexibility for design, etc. The PCF was first proposed by Philip Russell from the University of Bath, UK in the mid-nineties [2]. Its cross-sectional design consists of a number of air holes to form a unique lattice shape of hexagonal or circular structure to propagate the light signal through the central region of the PCFs. Intriguing optical characteristics of PCFs, i.e., their ability to hold a lower loss confinement in light wave guidance than the conventional optical fibres, have drawn plenty of attention in this research field. PCFs are also widely used for various applications, because it has been proven that by controlling and manipulating the cross-sectional structural parameters, namely, air hole diameter and the pitch length (gap between neighbouring holes), it is possible to engineer their optical characteristics [3].

Numerous techniques have been established in optical fibre sensing, such as fibre Bragg gratings (FBG) [4], multi-mode interface [5], resonant mirror [6], micro-ring resonators [7], polymer planar waveguides [8] and surface plasmon resonance (SPR) [9]. SPR-based sensing, as one of the most popular detecting techniques, has been widely used in applications such as medical

diagnostics, food testing, glucose monitoring, bioimaging, solution concentration measurement and antibody-antigen detection [10]. The principle used for most SPR sensing is the conventional Kretchmann SPR configuration. In this configuration, a coupling prism with a thin metal-deposited base is used in the presence of incident light at a specific angle. This incident light leads to the excitation of surface plasmons from the metal-dielectric interface whose wave vector parallel to the metal-dielectric surface matches that of the surface plasmon wave [11]. As mentioned before, the optimisation of PCF's structural parameters is a key feature/advantage of that kind of fibre. These parameters, including metal type, positioning, coating thickness and associated design with PCF, which are needed for SPR, can also be utilised to design different sensors for achieving various required specifications.

Relevant studies have been reported on fibre temperature sensing in the past few years. An isopropanol-filled PCF long period grating-based temperature sensor was proposed by C. Du et al. [12] for a temperature sensing range of 20–50 °C. Q. Liu et al. [13] reported a sensor on the principle of coupling between liquid core and defect mode having a comparatively wider sensing range of 20–80 °C and achieved a low temperature sensitivity of −1.85 nm/°C. A temperature sensitivity of −5.5 nm/°C was also reported by Y. Peng et al. [14] by using a bandgap-like effect on a selective liquid-filled PCF with a temperature detection range of 20–28 °C. Chen et al. [15] reported an ultracompact PCF-based temperature sensor with a maximum temperature sensitivity of 2.82 nm/°C. J. Zuo et al. [16] demonstrated an avoided-crossing-based selectively filled PCF temperature sensor and achieved a maximum temperature sensitivity of −6.9 nm/°C at 36.5 °C. Using Sagnac interference phenomena, the temperature sensitivity was improved up to 16.55 nm/°C in the measurement range from 45 °C to 75 °C by G. Wang et al. [17]. H. Liu et al. [18] also investigated a D-shaped temperature sensor with ethanol as a sensing medium and their analysis revealed a maximum temperature sensitivity of −1 nm/°C. Other types of PCF temperature sensors were also reported by Wang et al. [19] and others [20]. Photonic crystal fibre embedded between multimode fibres (MMF) by Wang et al., had limitations in the measurement of temperature between 35 °C to 100 °C [19], but it was reported in the paper that the length of the PCF had no influence on refractive index (RI) of the sensor and was thereby easy to fabricate.

In this paper, we present an optimised design structure of a multi-core PCF-SPR-based temperature sensor filled and sealed with either liquid ethanol or benzene as a temperature-sensitive material. In our proposed sensor design, we utilise the best of PCF and SPR technologies. Due to the exterior metal coating, it is easier and more economical to fabricate the proposed multicore PCF-SPR sensor using the available PCF fabrication and metal coating techniques reported in [9,21]. The host silica material that make up the cladding and core of the PCF is also considered to be temperature sensitive for the correct simulation and analysis of the temperature sensing performance. The performance of the proposed multi-core PCF-SPR sensor was analysed by finite elemental method (FEM) with COMSOL Multiphysics software and the results were analysed for a temperature range of 10–80 °C. Another advantage of this compact temperature sensor is its remarkable small size that could be suitably utilised in space-constrained temperature sensing and measurements applications. We envisage that the proposed temperature sensor will find wider applications in the fields of environmental and life sciences, manufacturing and medical devices because of the ease in fabrication of the proposed PCF structure and the excellent sensing performance after structural optimisation, which are also reported in this work.

2. Design and Numerical Method

The schematic cross-section of the proposed temperature sensor is illustrated in Figure 1. The PCF part of the sensor design consists of six cores that can detect the surrounding temperature changes through the ethanol or benzene (temperature sensing material) surrounding the PCF part coated with six segments of exterior metal coatings.
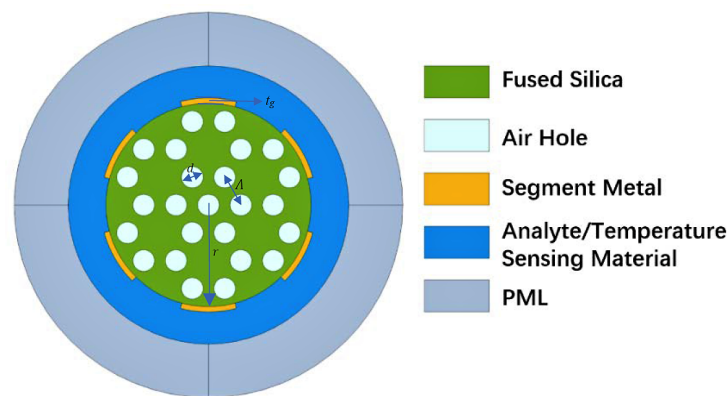
Figure 1. Schematic cross-section structure of the SPR-based photonic crystal fibre (PCF) temperature sensor with Λ = 3 μm, d = 2 μm, r = 9.5 μm and t_g = 50 nm.

2.1. Design Principles of the Two-Dimensional Fibre Sensor

Figure 1 shows the air-holes are arranged in a hexagonal lattice. The diameter of each air-hole (d) is 2 μm. These air-holes are used to obtain consummate coupling between surface plasmon polariton (SPP) mode(s) and core guided mode(s). The centre to centre distance between any two neighbouring air holes, pitch (Λ), is 3 μm. The entire fibre cross-section radius (r) is 9.5 μm; it forms the metal-coating(s) boundary height from the centre of the fibre. The thickness of the coated gold layer(s) (t_g) is 50 nm. The width of each segmented gold film is about 5 μm and the thickness of the analyte/temperature sensing material layer is set as 3 μm. Typical length of PCF-SPR sensors is in the range of 10–25 mm [22,23]. A perfectly matched layer (PML) is introduced around the temperature sensitive material to absorb incident radiation without producing any back reflections.

In our analysis we are comparing two different temperature-sensitive materials, ethanol and benzene, having refractive indexes lower and higher than silica (host material of the fibre) respectively, in order to deduce suitable applications for their unique properties.

2.2. Numerical Analysis

For this PCF temperature sensor, ethanol or benzene was independently used as the sensing medium. The fused silica is considered as the host material in this PCF sensor. Its wavelength-dependent RI equation is calculated by the Sellmeier equation [24]

$$n(\lambda) = \sqrt{1 + \frac{B_1{}^2}{\lambda^2 - C_1} + \frac{B_2{}^2}{\lambda^2 - C_2} + \frac{B_3{}^2}{\lambda^2 - C_3}} \tag{1}$$

where B_1 = 0.691663, B_2 = 0.407943, B_3 = 0.897479, C_1 = 0.004679 μm^2, C_2 = 0.013512 μm^2 and C_3 = 97.934003 μm^2. Here, the λ represents the incident light wavelength in free-space.

In order to get the actual value of the dielectric constant of gold, the Drude model was used [25]:

$$\varepsilon(\lambda) = 1 - \frac{\lambda^2 \lambda_c}{\lambda_p^2 (\lambda_c + i\lambda)} \tag{2}$$

where λ_p is the plasma wavelength and λ_c is the collision wavelength of the metal. In the case of gold, λ_p is 0.16826 μm and λ_c is 8.9342 μm [24].

The RI of the sensing medium (ethanol or benzene) used is dependent on both wavelength and temperature changes, and it is determined as follows [26–28],

$$n = n_0 + \frac{dn}{dT}(T - T_0) \tag{3}$$

where n_0 is the refractive index for ethanol or benzene at the reference value T_0 which depends on the wavelength and can be calculated using:

$$n_0^2 = 1 + \frac{0.0165\lambda^2}{(\lambda^2 - 9.08)} + \frac{0.8268\lambda^2}{(\lambda^2 - 0.01039)} \tag{4}$$

for ethanol [29], or

$$n_0^2 = 2.170184597 + 0.00059399\lambda^2 + 0.02303464\lambda^{-2} - 0.000499485\lambda^{-4} + 0.000178796\lambda^{-6} \tag{5}$$

for benzene [30]. The thermo optical co-efficient $\frac{dn}{dT}$ is $-3.94 \times 10^{-4}/°C$ or $-7.594 \times 10^{-4}/°C$ at reference temperature $T_0 = 20\,°C$ or $27\,°C$ for ethanol and benzene respectively.

The confinement loss is determined by the equation,

$$\alpha_{\text{loss}} = 8.686 \times \frac{2\pi}{\lambda}\Im(n_{\text{eff}}) \times 10^4, \tag{6}$$

where $\Im(n_{\text{eff}})$ is the imaginary part of the effective refractive index.

This temperature sensor has been designed to have a metal layer of six segmented gold films around the fibre. This is to prevent higher order surface plasmons generated from the metal surface affecting the main sensing layer (see Figure 1). Chemical vapour deposition (CVD) method is suggested as the best way of coating considering its cost effectiveness and practicality compared to other normal external metal coatings on nonlinear surfaces [9].

3. FEM Simulation Results and Discussion

The sensor performance of this PCF sensor was studied in terms of temperature sensitivity, resolution, figure of merit (FOM) and linearity of confinement loss peak wavelength. The detection range chosen to investigate the temperature sensing performance of the PCF sensor is 10 °C to 80 °C.

3.1. Modal Analysis

The electric field distribution (cross-sectional light signal electric power concentration) of the core-guided fundamental mode, plasmon mode and phase matching mode is shown in Figure 2. A finite element method was utilised to calculate the complex propagation constants of the core-guided and surface plasmon polariton (SPP) mode.

Results show that there is a significant positive correlation between the real effective refractive index (n_{eff}) of the fundamental core mode and the SPP mode. Surface plasmon modes were generated as a result of these modes coupling at a particular wavelength (1922.7 nm). At this wavelength, the maximum energy is transferred from the core mode to the SPP mode due to the excitation of the free electrons from the segmented gold layer(s). This particular wavelength is known as the resonance wavelength that is termed as the phase-matching point. Figure 2 shows electric field distributions of the temperature sensor with ethanol as the sensitive material at the core guided fundamental mode (1400 nm), phase-matching point (1922.7 nm), higher-wavelength guided mode (2300 nm) and surface plasmon polariton mode (1922.7 nm).

Figure 3 shows the dispersion relations of the real (n_{eff}) and fundamental modes and the plasmon mode at $T = 40\,°C$ with ethanol as the temperature-sensitive material. It was observed in Figure 3 that the coupling point, the effective refractive index of the fundamental core guided mode and the SPP mode is the same but the imaginary part (confinement loss) is different. Therefore, it can be claimed that the proposed PCF sensor has phase matching and incomplete coupling. An incomplete coupling happens when two coupling modes have equal real parts of effective refractive indices but different imaginary parts [31]. A similar observation was reported in the literature [32].
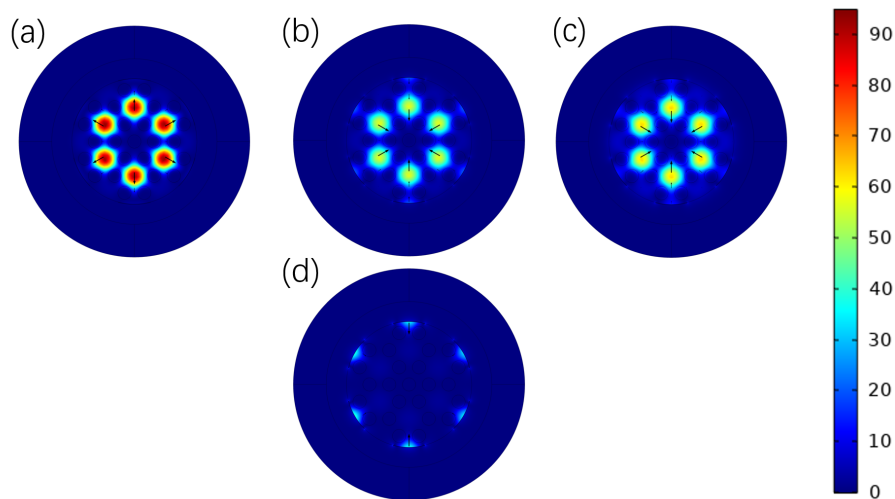
Figure 2. Electric field distributions of the proposed temperature sensor with ethanol as the sensitive material for core-guided fundamental mode at (**a**) shorter wavelength (1400 nm), (**b**) resonance wavelength (1922.7 nm), (**c**) longer wavelength (2300 nm) and (**d**) the surface plasmon polariton mode at resonance wavelength (1922.7 nm), respectively (ambient temperature = 40 °C).
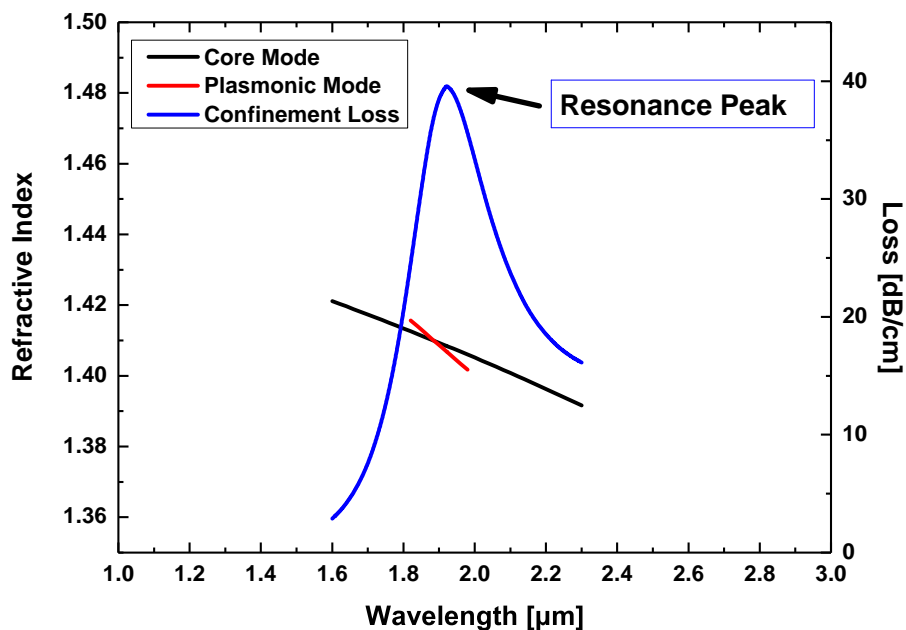

Figure 3. Dispersion relations of the core-guided mode and the plasmon mode at $T = 40$ °C with ethanol as the temperature sensitive material (where electric field distributions of the core-guided and plasmon modes are shown in the inset).

Figures 4 and 5 show that, due to the temperature variation, the RI of the temperature sensitive liquid (ethanol/benzene) changes which leads to the change in the resonance wavelength. This affects the core-cladding index contrast which changes the resonance wavelength. Using ethanol (a lower RI material compared to silica) as the sensing medium, an increase of temperature causes the steady shift of the resonance wavelength peak to lower wavelengths (see Figure 4); similar results were already reported in [33]. This steady shift reduces the confinement loss in the core mode, thereby increasing the light confinement in the sensor. On the other hand, different dynamics were observed while using benzene (a higher RI material compared to silica). Here, increasing the temperature in the range from 50 °C to 70 °C causes the resonance wavelength to shift to longer wavelength (see Figure 5b); similar results were already reported in [34,35] for microstructured optical fibre-based surface plasmon

resonance (MOF-SPR) sensors. A further increase to 80 °C shifted the resonance wavelength to a lower wavelength because the RI of benzene at this temperature becomes lower than the RI of the host material (silica) as it approaches the boiling point of benzene [32].
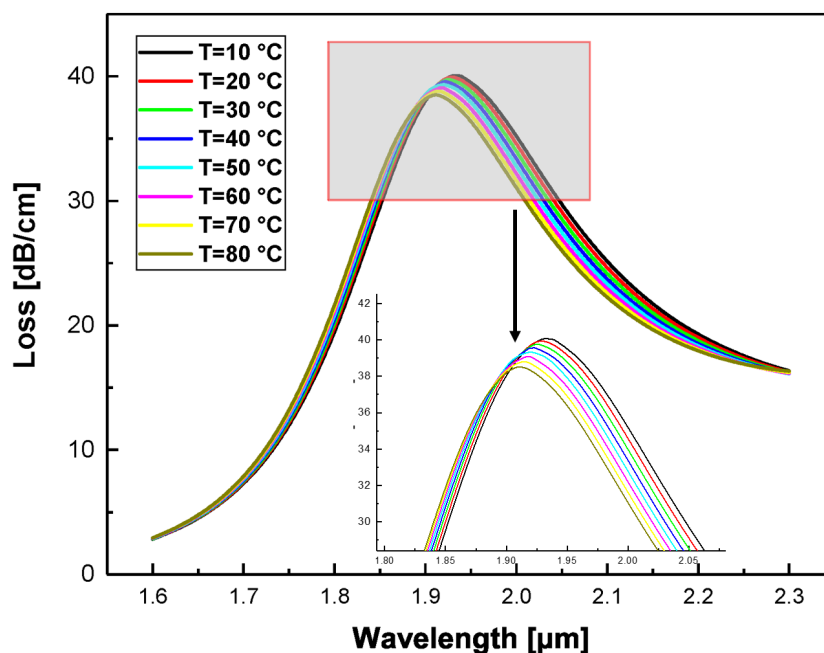

Figure 4. Confinement loss as a function of wavelength in the temperature range from 10 °C to 80 °C in steps of 10 °C when ethanol is used as the temperature sensitive material.
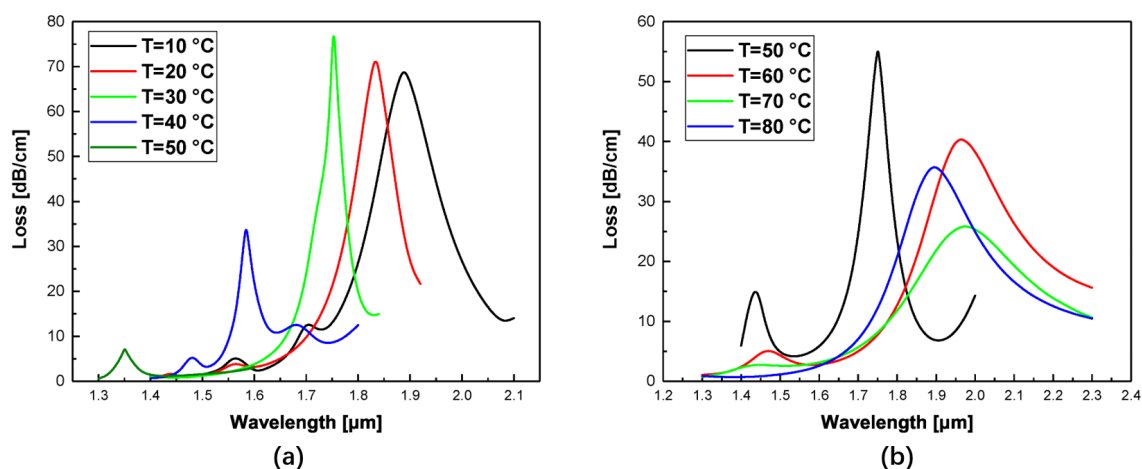

(a)   (b)

Figure 5. Confinement loss as a function of wavelength in the temperature range from (**a**) 10 °C to 50 °C; (**b**) 50 °C to 80 °C with benzene as the temperature sensitive material.

However, it should be noted that the resonance wavelength in Figure 5a shifts to the lower wavelength side as the temperature increases in the low temperature range (10 °C to 50 °C). Two different dynamics were observed for 10 °C to 50 °C and 50 °C to 80 °C for the benzene-based sensor due to the selection of the resonance peak for the SPR process. As it is illustrated in Figure 6, for the temperature range from 40 °C to 50 °C, there are two resonance peaks which caused by fundamental SPR (peak 1) and higher order SPR (peak 2), respectively. Due to higher wavelength shift of peak 1, it was selected as the main resonance peak for sensing. However, when temperature is up to 50 °C, the obtained confinement loss value of peak 1 was found to be less than 10 dB/cm which is too low to be detected by optical spectrum analyser. Therefore, peak 2 was selected for the higher temperature range (50–80 °C) to be used as the resonance peak for temperature sensing.

This also explains why for benzene-based temperature sensor, there are two temperature ranges of the corresponding confinement loss spectrum.
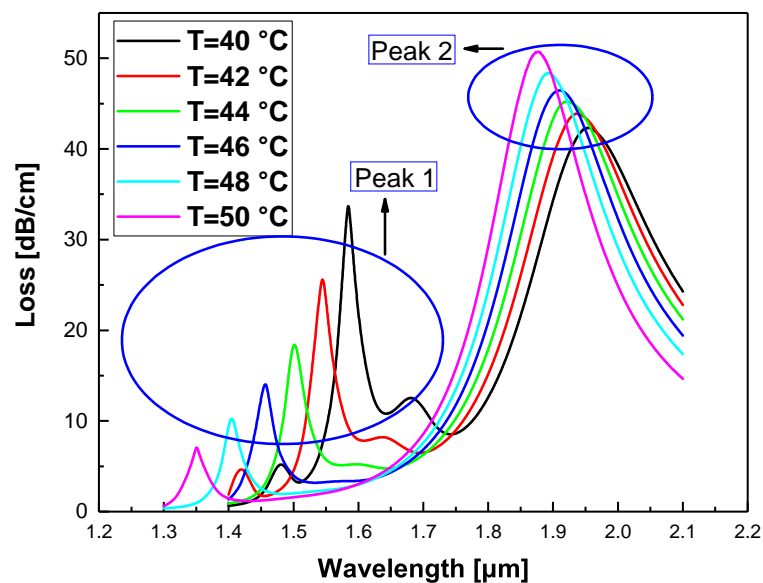

Figure 6. Confinement loss as a function of wavelength in the temperature range from 40 °C to 50 °C in a step of 2 °C with benzene as the temperature sensitive material.

3.2. Sensitivity

Temperature sensing was thereby accomplished based on the shifts in the resonance wavelength (peak location of the loss characteristics). The temperature sensitivity was calculated by [26–28]:

$$S\left[\frac{nm}{°C}\right] = \Delta\lambda_{peak}/\Delta T, \qquad (7)$$

where $\Delta\lambda_{peak}$ and ΔT indicate propagation peak wavelength difference and temperature variation, respectively.

The maximum temperature sensitivity obtained for this temperature sensor is 360 pm/°C or 23.3 nm/°C for ethanol or benzene, respectively (see Tables 1 and 2).

Table 1. Sensing performance of the proposed multi-core PCF-based SPR sensor (using ethanol as the sensitive material) in the temperature range from 10 °C to 80 °C.

S/N	Temp. [°C]	Reso. Wavelength [nm]	n_{eff}	Conf. Loss [dB/cm]	$\partial\lambda_{peak}$ [nm]	Temp. Sensitivity [nm/°C]	Resolution [°C]
1	10	1932.9	1.4080	40.0658	N/A	N/A	N/A
2	20	1929.3	1.4081	39.9305	3.6	0.36	2.78×10^{-1}
3	30	1926.1	1.4083	39.7599	3.2	0.32	3.12×10^{-1}
4	40	1922.7	1.4084	39.5594	3.4	0.34	2.94×10^{-1}
5	50	1919.6	1.4085	39.3323	3.1	0.31	3.23×10^{-1}
6	60	1916.7	1.4086	39.0815	2.9	0.29	3.45×10^{-1}
7	70	1913.8	1.4088	38.8091	2.9	0.29	3.45×10^{-1}
8	80	1911.3	1.4089	38.5164	2.5	0.25	4.00×10^{-1}

Table 2. Sensing performance of the proposed multi-core PCF-based SPR sensor (using benzene as the sensitive material) in the temperature range from 10 °C to 80 °C.

S/N	Temp. [°C]	Reso. Wavelength [nm]	n_{eff}	Conf. Loss [dB/cm]	$\partial\lambda_{peak}$ [nm]	Temp. Sensitivity [nm/°C]	Resolution [°C]
1	10	1888	1.4094	68.7349	N/A	N/A	N/A
2	20	1834	1.4117	71.0958	54.00	5.4	1.85×10^{-2}
3	30	1754	1.415	76.8213	80.00	8	1.25×10^{-2}
4	40	1584	1.4215	33.6976	170.00	17	5.88×10^{-3}
5 *	50	1351	1.4298	7.0533	233	23.3	4.29×10^{-3}
5 **	50	1751	1.4154	54.9956	N/A	N/A	N/A
6	60	1964	1.4067	40.3456	−213	−21.3	-4.69×10^{-3}
7	70	1975	1.4062	25.8258	−11	−1.1	-9.09×10^{-2}
8	80	1896	1.4095	35.6852	79	7.9	1.27×10^{-2}

[*] Resonance wavelength for peak 1 at 50 °C. [**] Resonance wavelength for peak 2 at 50 °C.

3.3. Resolution

The resolution of the proposed temperature sensor specifies the measure at which this sensor will detect the smallest temperature variation. It can be expressed as [27],

$$S_R[°C] = \partial T \times \frac{\partial\lambda_{min}}{\partial\lambda_{peak}} \tag{8}$$

where $\partial\lambda_{min}$, ∂T and $\partial\lambda_{peak}$ indicate minimum wavelength resolution, temperature difference and light signal peak wavelength difference respectively. Using $\partial\lambda_{min}$ = 0.1 nm in Equation (8), the maximum resolution calculated is 2.78×10^{-1} °C or 4.29×10^{-3} °C with a step size of 10 °C, using ethanol or benzene, respectively. We noticed that the proposed sensor could detect the smallest temperature change in the order of 10^{-3}.

3.4. Optimisation of the Sensor Structural Parameters

The proposed temperature sensor was basically designed with Λ = 3 µm, d = 2 µm and t_g = 50 nm. Each of those parameters was varied to get the optimised performance that could be achieved by the proposed temperature sensor using ethanol as the temperature-sensing material due to the good linearity in the measurement range.

Figure 7 shows how the thickness of the segmented gold layer(s) was varied from 50 nm to 30 nm and 80 nm for temperature values of 10 °C and 20 °C. It was noticed that with a reduction of t_g to 30 nm, there was an increase in the value of the confinement loss peak. This was due to the lower damping loss of the metal layer [32]. Additionally, it was noticed that the increase of the gold coating thickness to 80 nm also increases the confinement loss. Therefore, the gold thickness chosen at 50 nm gives the best sensitivity with the least confinement loss.

Figure 8 shows how the gap between two adjacent air-holes (Λ) can be varied to get the optimised dimension. Here, the pitch is varied by ± 5% of its original distance for temperature 10 °C and 20 °C. It can be seen that the confinement loss characteristics of the proposed temperature sensor increases when the pitch is reduced. However, the wavelength shift is also increased in the process, leading to an increase in sensitivity. The optimised pitch can be 2.85 µm, which gives the best sensitivity from the sensor.
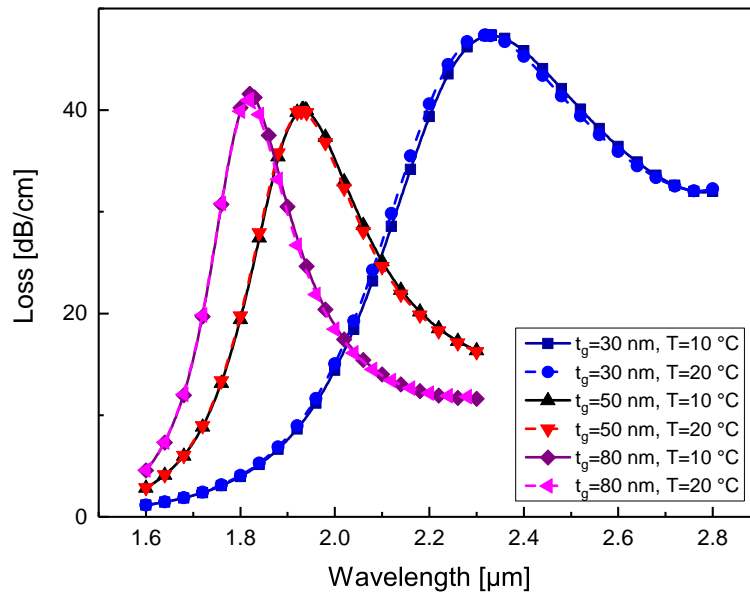
Figure 7. Confinement loss characteristics at temperatures 10 °C and 20 °C with different values of gold thickness, t_g.
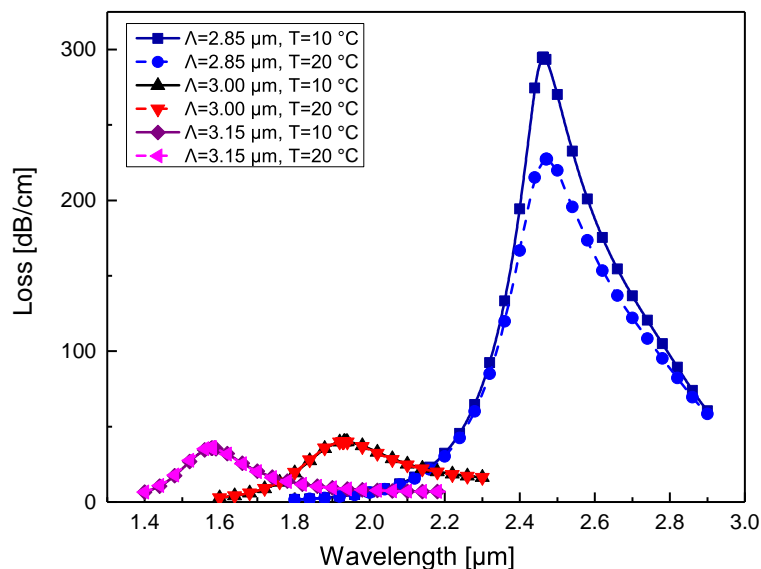

Figure 8. Confinement loss characteristics at temperatures 10 °C and 20 °C with different values of pitch, Λ .

Figure 9 shows the confinement loss characteristics of the proposed temperature sensor with different diameters of the air-hole. This was carried out to get the optimised air-hole diameter for the best sensor sensitivity. The air-hole diameter was varied by $\pm$ 5% of the initial value for temperatures 10 °C and 20 °C. It can be seen that the confinement loss characteristics of the proposed temperature sensor increase when the air-hole diameter is reduced, which leads to an increase in sensitivity because of the wavelength shift to longer wavelength. Here, more openings for the evanescent field are made available for the interaction with the gold layer, which causes the increase in the confinement loss, as noticed. Therefore, the optimised air-hole diameter can be 1.9 μm, which gives the best sensitivity from the temperature sensor.
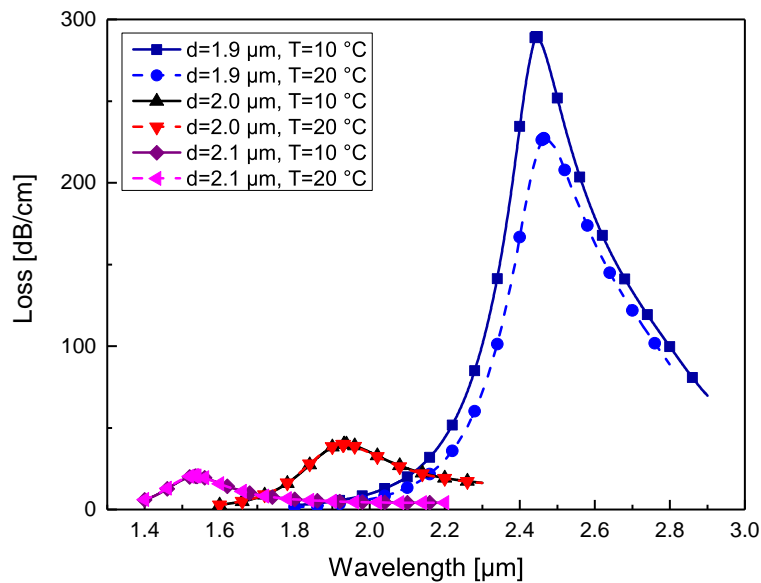
Figure 9. Confinement loss characteristics at temperatures 10 °C and 20 °C with different values of air-hole diameter, d.

The outside metal coating of the whole fibre for sensor design has been proposed in [36]. The results with this coating scheme are illustrated in Figure 10 (dotted line) and also compared with the results of the reported six segmented coating scheme (solid line) with ethanol or benzene.
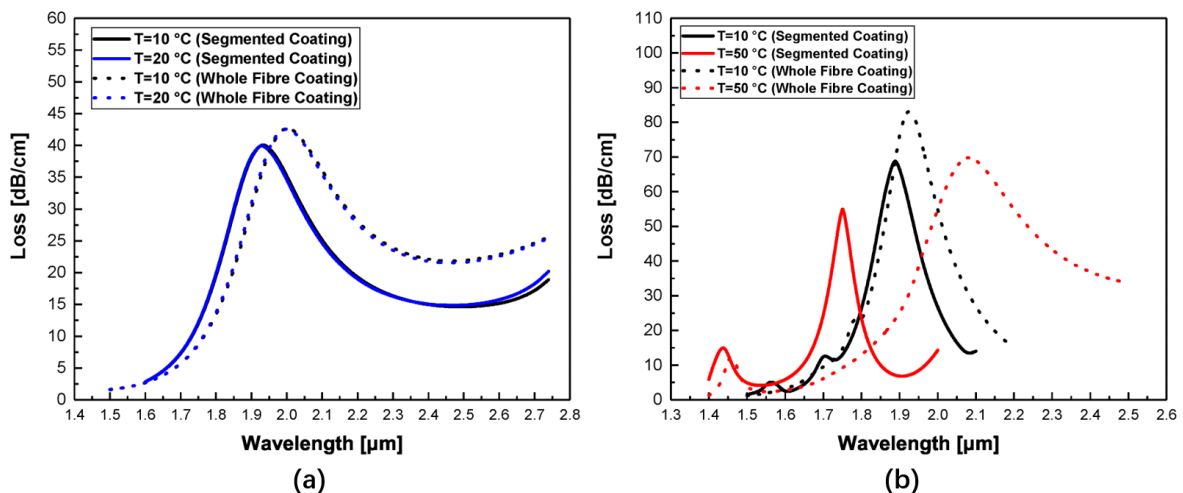

Figure 10. Confinement loss comparisons of segmented coating and whole fibre coating schemes at temperatures of (**a**)10 °C and 20 °C with the ethanol-based sensor and (**b**) 10 °C and 50 °C with the benzene-based sensor.

As can be seen from Figure 10a, there is no conspicuous difference between the two coating schemes. According to the results of numerical analysis, the wavelength shift for the whole fibre coating sensor from 10 °C to 20 °C is 2 nm which is lower than the six segmented coating scheme with the wavelength shift of 3.6 nm.

For the benzene-based temperature sensor illustrated in Figure 10b, the increment in the value of confinement loss is higher than for the ethanol-based temperature sensor. The reason is because benzene has a higher refractive index than the fused silica and more transmitted light energy would be absorbed by the whole fibre coated metal layer by the SPR phenomenon. From the simulation results, the wavelength shift of the benzene-based temperature sensor with a whole fibre coating was also found to be lower than for the segmented coating scheme (35 nm < 54 nm) from 10 °C to 20 °C.

Additionally, the loss spectra at temperature 50 °C of the benzene-based sensor with the proposed segmented coating shows a more sharp resonance curve (red solid line in Figure 10b) compared to the one with the whole fibre coating scheme (red dotted line in Figure 10b). Hence, the six segmented coating scheme would be a better choice of metal coating compared with whole fibre coating scheme as it can provide higher sensitivities and more sharp loss spectra.

3.5. Sensitivity Comparison of the Proposed Temperature Sensor with Ethanol or Benzene

This work investigated the sensing performances of two temperature-sensitive materials (ethanol or benzene) in the proposed PCF-SPR sensor. From the obtained results we can conclude that benzene works as a better sensing medium than ethanol within the measurement range of 10 °C to 50 °C (see Figure 11a). On the other hand, ethanol as the sensing medium showed more steady sensing performance over the entire measurement range of 10 °C to 80 °C, as Figure 11 depicts.
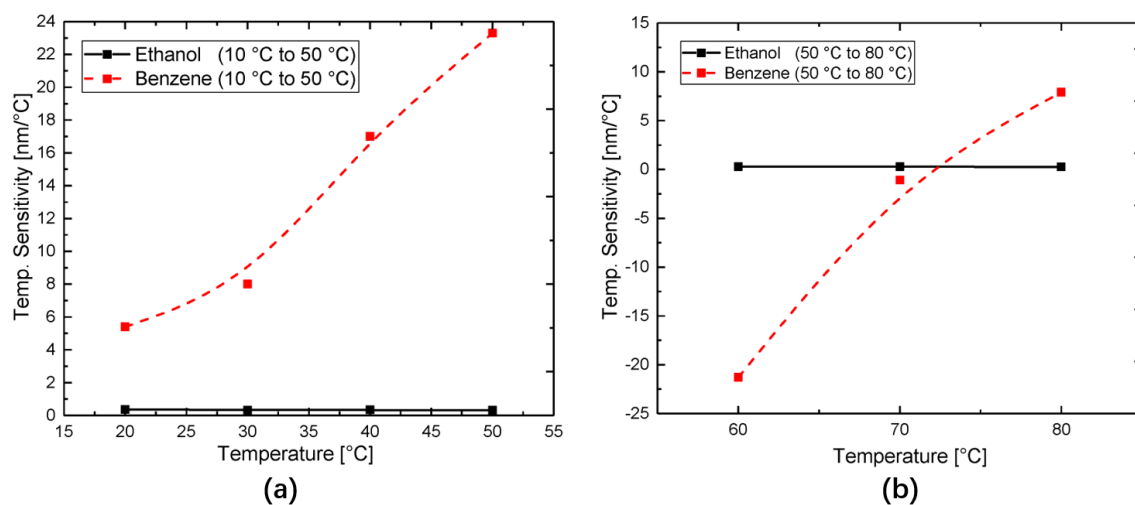

Figure 11. Sensitivity in the detection ranges from (**a**) 10 °C to 50 °C and (**b**) 50 °C to 80 °C with two different temperature sensing materials.

The quality of any sensor's performance depends on the linearity response of the regression line [37]. Figure 12a shows the linear response with value R^2 is 0.99757 of the ethanol-based temperature sensor, which shows good linearity but low sensitivity. Figure 12b shows the linear responses of the benzene-based temperature sensor for 10 °C to 50 °C and 50 °C to 80 °C. According to the simulation results, the maximum resonance wavelength was found to be 1984 nm when the temperature is 69 °C; then it will have a blue shift to the lower wavelength for higher temperature. Here, the sensor shows good linearity and low sensitivity for temperatures below 50 °C while for the 50 °C to 80 °C range, it provides better sensitivity for a small temperature sensing range 50 °C to 60 °C but also shows very poor linearity. Hence, in reality, the recommended temperature sensing range of the benzene-based sensor is from 10 °C to 50 °C.

Figure of merit (FOM) is another parameter used to measure the performance of sensors. It is calculated as [15],

$$\text{FOM} = \frac{\text{S}}{\text{FWHM}} \tag{9}$$

where S and FWHM indicate temperature sensitivity (nm/°C) and full width at half maximum of the transmission dip (nm) respectively.

From Equation (9), the maximum FOM of 0.000957/°C or 0.3963/°C was reported for sensing with ethanol or benzene filled temperature sensor, respectively. Therefore, the detection accuracy of the benzene-temperature sensor gives a better performance within the small measurement range of 10–50 °C.
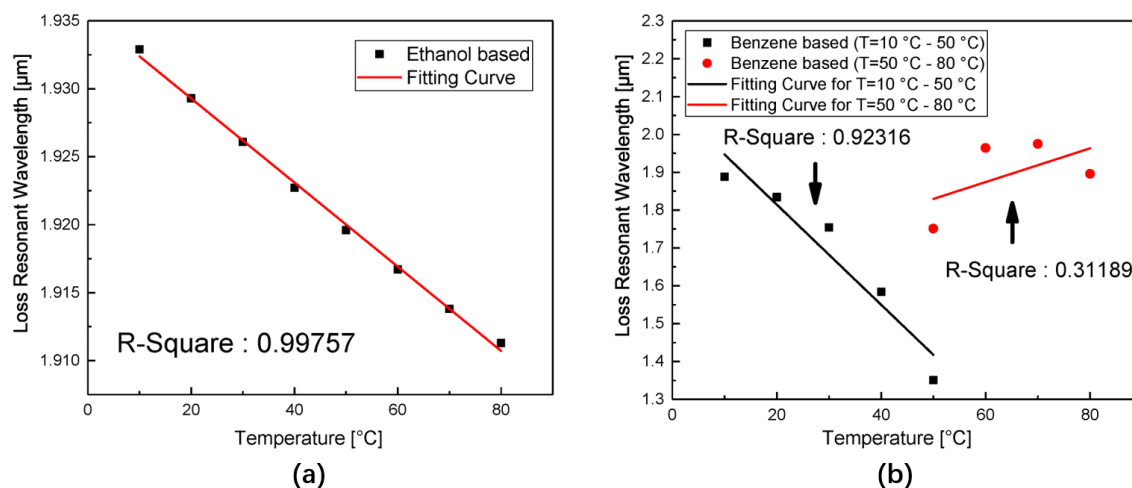
Figure 12. Resonance wavelength and the temperature changes between (**a**) 10–80 °C using ethanol as the sensing medium and (**b**) 10–50 °C, and 50–80 °C using benzene as the sensing medium.

Table 3 shows the comparison of some earlier reported sensors with the proposed segmented gold-coated multi-core PCF-based SPR temperature sensor. The sensitivity shown by the benzene filled temperature sensor (23.3 nm/°C) for a specific temperature measurement range (10 °C to 50 °C) is at least one order of magnitude higher than the other reported sensors.

Table 3. Sensing performance comparison of the proposed sensor with previously reported sensors.

Sensor Type	Temperature Sensing Material	Temperature Sensing Range [°C]	Maximum Sensitivity [nm/°C]	Year
FBG [38]	Zinc	35–80	0.0496	2006
SPR [27]	Liquid(RI = 1.35)	0–100	0.72	2012
SPR [26]	Ethanol and chloroform	−20–58	5.6	2014
SPR [39]	Anhydrous Ethanol	35–70	1.5745	2015
LPFG [40]	Poly-dimethylsiloxane	20–80	0.2554	2016
HCF [41]	Graphene Quantum Dots	10–80	0.1237	2017
PMF [42]	CdSe Quantum Dot	25–48	0.0585	2017
PCF-LPG [12]	Isopropanol	20–50	1.356	2017
MMF-PCF-MMF [19]	Gold-PDMS	35–100	−1.551	2018
Proposed sensor	Ethanol	10–80	0.36	2020
Proposed sensor	Benzene	10–50	23.3	2020

4. Conclusions

In conclusion, a novel segmented outer-surface metal-coated multi-core PCF-based SPR temperature sensor has been designed. The temperature-sensitive materials (ethanol or benzene) used were compared. The segmented gold layers were introduced to reduce the higher order surface plasmons for less sub-peak effect [43]. The maximum sensitivity of the ethanol-based temperature sensor is low compared to the benzene-based temperature sensor but shows good linearity all through the measurement range of 10–80 °C. The results show that the resonance wavelength shift is sensitive to temperature variation. Optimisation of the structural parameters can further increase the sensitivity of the sensor as observed from the simulation results. Based on the above comprehensive discussion and analysis on the proposed PCF-SPR sensor with its advantages of simple design structure and ease of metal coating (outside the optical fibre), we are of the opinion that these sensors with different sensing materials could be applied to meet different temperature sensing needs and requirements.

References

1. Addanki, S.; Amiri, I.; Yupapin, P. Review of optical fibers-introduction and applications in fiber lasers. *Results Phys.* **2018**, *10*, 743–750. [CrossRef]

2. Gangopadhyay, T.K.; Kumbhakar, P.; Mandal, M.K. *Photonics and Fiber Optics: Foundations and Applications*; CRC Press: Boca Raton, FL, USA, 2019.

3. Wu, D.K.C.; Kuhlmey, B.T.; Eggleton, B.J. Ultrasensitive photonic crystal fiber refractive index sensor. *Opt. Lett.* **2009**, *34*, 322–324. [CrossRef] [PubMed]

4. Hammon, T.; Stokes, A. Optical fibre bragg grating temperature sensor measurements in an electrical power transformer using a temperature compensated optical fibre bragg grating as a reference. In *Optical Fiber Sensors*; Optical Society of America: Washington, DC, USA, 1996; p. Th337; doi:10.1364/OFS.1996.Th337. [CrossRef]

5. Irace, A.; Breglio, G. All-silicon optical temperature sensor based on Multi-Mode Interference. *Opt. Express* **2003**, *11*, 2807–2812. [CrossRef] [PubMed]

6. Buckle, P.; Davies, R.; Kinning, T.; Yeung, D.; Edwards, P.; Pollard-Knight, D.; Lowe, C. The resonant mirror: A novel optical sensor for direct sensing of biomolecular interactions part II: Applications. *Biosens. Bioelectron.* **1993**, *8*, 355–363. [CrossRef]

7. Kim, H.T.; Yu, M. Cascaded ring resonator-based temperature sensor with simultaneously enhanced sensitivity and range. *Opt. Express* **2016**, *24*, 9501–9510. [CrossRef] [PubMed]

8. Jung, W.G.; Kim, S.W.; Kim, K.T.; Kim, E.S.; Kang, S.W. High-sensitivity temperature sensor using a side-polished single-mode fiber covered with the polymer planar waveguide. *IEEE Photonics Technol. Lett.* **2001**, *13*, 1209–1211. [CrossRef]

9. Rifat, A.A.; Ahmed, R.; Yetisen, A.K.; Butt, H.; Sabouri, A.; Mahdiraji, G.A.; Yun, S.H.; Adikan, F.M. Photonic crystal fiber based plasmonic sensors. *Sens. Actuators B Chem.* **2017**, *243*, 311 – 325. [CrossRef]

10. Momota, M.R.; Hasan, M.R. Hollow-core silver coated photonic crystal fiber plasmonic sensor. *Opt. Mater.* **2018**, *76*, 287–294. [CrossRef]

11. Hoa, X.; Kirk, A.; Tabrizian, M. Towards integrated and sensitive surface plasmon resonance biosensors: A review of recent progress. *Biosens. Bioelectron.* **2007**, *23*, 151–160. [CrossRef]

12. Du, C.; Wang, Q.; Zhao, Y.; Li, J. Highly sensitive temperature sensor based on an isopropanol-filled photonic crystal fiber long period grating. *Opt. Fiber Technol.* **2017**, *34*, 12–15. [CrossRef]

13. Liu, Q.; Li, S.; Chen, H.; Fan, Z.; Li, J. Photonic Crystal Fiber Temperature Sensor Based on Coupling Between Liquid-Core Mode and Defect Mode. *IEEE Photonics J.* **2015**, *7*, 1–9. [CrossRef]

14. Peng, Y.; Hou, J.; Zhang, Y.; Huang, Z.; Xiao, R.; Lu, Q. Temperature sensing using the bandgap-like effect in a selectively liquid-filled photonic crystal fiber. *Opt. Lett.* **2013**, *38*, 263–265. [CrossRef] [PubMed]

15. Chen, H.; Li, S.; Li, J.; Han, Y.; Wu, Y. High Sensitivity of Temperature Sensor Based on Ultracompact Photonics Crystal Fibers. *IEEE Photonics J.* **2014**, *6*, 1–6. [CrossRef]

16. Zuo, J.; Han, T.; Yang, J.; Chen, Y.; Lin, Y.; Cai, J. High Sensitivity Temperature Sensor With an Avoided-Crossing Based Selective-Filling High Birefringent Photonic Crystal Fiber Sagnac Interferometer. *IEEE Access* **2018**, *6*, 45527–45533. [CrossRef]

17. Wang, G.; Lu, Y.; Yang, X.; Duan, L.; Yao, J. Square-lattice alcohol-filled photonic crystal fiber temperature sensor based on a Sagnac interferometer. *Appl. Opt.* **2019**, *58*, 2132–2136. [CrossRef]

18. Liu, H.; Li, H.; Wang, Q.; Wang, M.; Ding, Y.; Zhu, C. Simultaneous measurement of temperature and magnetic field based on surface plasmon resonance and Sagnac interference in a D-shaped photonic crystal fiber. *Opt. Quantum Electron.* **2018**, *50*, 392. [CrossRef]

19. Wang, Y.; Huang, Q.; Zhu, W.; Yang, M.; Lewis, E. Novel optical fiber SPR temperature sensor based on MMF-PCF-MMF structure and gold-PDMS film. *Opt. Express* **2018**, *26*, 1910–1917. [CrossRef]

20. Canovi, M.; Lucchetti, J.; Stravalaci, M.; Re, F.; Moscatelli, D.; Bigini, P.; Salmona, M.; Gobbi, M. Applications of Surface Plasmon Resonance (SPR) for the Characterization of Nanoparticles Developed for Biomedical Purposes. *Sensors* **2012**, *12*, 16420–16432. [CrossRef]

21. Gandhi, M.S.A.; Chu, S.; Senthilnathan, K.; Babu, P.R.; Nakkeeran, K.; Li, Q. Recent Advances in Plasmonic Sensor-Based Fiber Optic Probes for Biological Applications. *Appl. Sci.* **2019**, *9*, 949. [CrossRef]

22. Hassani, A.; Skorobogatiy, M. Design of the Microstructured Optical Fiber-based Surface Plasmon Resonance sensors with enhanced microfluidics. *Opt. Express* **2006**, *14*, 11616–11621. [CrossRef]

23. Chu, S.; Nakkeeran, K.; Abobaker, A.M.; Aphale, S.S.; Sivabalan, S.; Babu, P.R.; Senthilnathan, K. A Surface Plasmon Resonance Bio-Sensor based on Dual Core D-Shaped Photonic Crystal Fibre Embedded with Silver Nanowires for Multi-Sensing. *IEEE Sens. J.* **2020**. [CrossRef]

24. Mishra, A.K.; Mishra, S.K.; Verma, R.K. Graphene and Beyond Graphene MoS2: A New Window in Surface-Plasmon-Resonance-Based Fiber Optic Sensing. *J. Phys. Chem. C* **2016**, *120*, 2893–2900, doi:10.1021/acs.jpcc.5b08955. [CrossRef]

25. Zainuddin, N.; Ariannejad, M.; Arasu, P.; Harun, S.; Zakaria, R. Investigation of cladding thicknesses on silver SPR based side-polished optical fiber refractive-index sensor. *Results Phys.* **2019**, *13*, 102255. [CrossRef]

26. Luan, N.N.; Wang, R.; Lu, Y.; Yao, J. Simulation of surface plasmon resonance temperature sensor based on liquid mixture-filling microstructured optical fiber. *Opt. Eng.* **2014**, *53*, 1–4. [CrossRef]

27. Peng, Y.; Hou, J.; Huang, Z.; Lu, Q. Temperature sensor based on surface plasmon resonance within selectively coated photonic crystal fiber. *Appl. Opt.* **2012**, *51*, 6361–6367. [CrossRef]

28. Luan, N.; Wang, R.; Lv, W.; Lu, Y.; Yao, J. Surface Plasmon Resonance Temperature Sensor Based on Photonic Crystal Fibers Randomly Filled with Silver Nanowires. *Sensors* **2014**, *14*, 16035–16045. [CrossRef]

29. Sani, E.; Dell'Oro, A. Spectral optical constants of ethanol and isopropanol from ultraviolet to far infrared. *Opt. Mater.* **2016**, *60*, 137–141. [CrossRef]

30. Moutzouris, K.; Papamichael, M.; Betsis, S.C.; Stavrakas, I.; Hloupis, G.; Triantis, D. Refractive, dispersive and thermo-optic properties of twelve organic solvents in the visible and near-infrared. *Appl. Phys. B* **2014**, *116*, 617–622. [CrossRef]

31. Shuai, B.; Xia, L.; Zhang, Y.; Liu, D. A multi-core holey fiber based plasmonic sensor with large detection range and high linearity. *Opt. Express* **2012**, *20*, 5974–5986. [CrossRef]

32. Mollah, M.A.; Islam, S.R.; Yousufali, M.; Abdulrazak, L.F.; Hossain, M.B.; Amiri, I. Plasmonic temperature sensor using D-shaped photonic crystal fiber. *Results Phys.* **2020**, *16*, 102966. [CrossRef]

33. Li, X.G.; Zhao, Y.; Zhou, X.; Cai, L. High sensitivity all-fiber Sagnac interferometer temperature sensor using a selective ethanol-filled photonic crystal fiber. *Instrum. Sci. Technol.* **2018**, *46*, 253–264, doi:10.1080/10739149.2017.1380038. [CrossRef]

34. Liu, B.H.; Jiang, Y.X.; Zhu, X.S.; Tang, X.L.; Shi, Y.W. Hollow fiber surface plasmon resonance sensor for the detection of liquid with high refractive index. *Opt. Express* **2013**, *21*, 32349–32357. [CrossRef] [PubMed]

35. Luan, N.; Yao, J. High Refractive Index Surface Plasmon Resonance Sensor Based on a Silver Wire Filled Hollow Fiber. *IEEE Photonics J.* **2016**, *8*, 1–9. [CrossRef]

36. Rifat, A.; Mahdiraji, G.A.; Shee, Y.; Shawon, M.J.; Adikan, F.M. A Novel Photonic Crystal Fiber Biosensor Using Surface Plasmon Resonance. *Procedia Eng.* **2016**, *140*, 1–7. [CrossRef]

37. Hossen, M.N.; Ferdous, M.; Khalek, M.A.; Chakma, S.; Paul, B.K.; Ahmed, K. Design and analysis of biosensor based on surface plasmon resonance. *Sens. Bio-Sens. Res.* **2018**, *21*, 1–6. [CrossRef]

38. Li, Y.; Wang, Y.; Wen, C. Temperature and strain sensing properties of the zinc coated FBG. *Optik* **2016**, *127*, 6463–6469. [CrossRef]

39. Zhao, Y.; Deng, Z.; Hu, H. Fiber-Optic SPR Sensor for Temperature Measurement. *IEEE Trans. Instrum. Meas.* **2015**, *64*, 3099–3104. [CrossRef]

40. Wang, Q.; Du, C.; Zhang, J.; Lv, R.; Zhao, Y. Sensitivity-enhanced temperature sensor based on PDMS-coated long period fiber grating. *Opt. Commun.* **2016**, *377*, 89–93. [CrossRef]

41. Zhao, Y.; Tong, R.; Chen, M.; Xia, F. Fluorescence Temperature Sensor Based on GQDs Solution Encapsulated in Hollow Core Fiber. *IEEE Photonics Technol. Lett.* **2017**, *29*, 1544–1547. [CrossRef]

42. Irawati, N.; Harun, S.W.; Rahman, H.A.; Chong, S.S.; Hamizi, N.A.; Ahmad, H. Temperature sensing using CdSe quantum dot doped poly(methyl methacrylate) microfiber. *Appl. Opt.* **2017**, *56*, 4675–4679. [CrossRef]

43. Chu, S.; Nakkeeran, K.; Abobaker, A.M.; Aphale, S.S.; Sivabalan, S.; Babu, P.R.; Senthilnathan, K. Influence of the Sub-peak of Secondary Surface Plasmon Resonance onto the Sensing Performance of a D-shaped Photonic Crystal Fibre Sensor. *IEEE Sens. J.* **2019**. [CrossRef]